Wave Setup over a Fringing Reef with Large Bottom Roughness

MARK L. BUCKLEY AND RYAN J. LOWE

School of Earth and Environment, and The Oceans Institute, and ARC Centre of Excellence for Coral Reef Studies, University of Western Australia, Crawley, Western Australia, Australia

JEFF E. HANSEN

School of Earth and Environment, and The Oceans Institute, University of Western Australia, Crawley, Western Australia, Australia

AP R. VAN DONGEREN

Unit ZKS, Department AMO, Deltares, Delft, Netherlands

(Manuscript received 3 August 2015, in final form 18 March 2016)

ABSTRACT

The effect of bottom roughness on setup dynamics was investigated using high-resolution observations across a laboratory fringing reef profile with roughness elements scaled to mimic the frictional wave dissipation of a coral reef. Results with roughness were compared with smooth bottom runs across 16 offshore wave and still water level conditions. The time-averaged and depth-integrated force balance was evaluated from observations collected at 17 locations along the flume and consisted of cross-shore pressure and radiation stress gradients whose sum was balanced by quadratic mean bottom stresses. The introduction of roughness had two primary effects. First, for runs with roughness, frictional wave dissipation occurred on the reef slope offshore of the breakpoint, reducing wave heights prior to wave breaking. Second, offshore-directed mean bottom stresses were generated by the interaction of the combined wave–current velocity field with the roughness elements. These two mechanisms acted counter to one another. Frictional wave dissipation resulted in radiation stress gradients that were predicted to generate 18% (on average) less setup on the reef flat for rough runs than for smooth runs when neglecting mean bottom stresses. However, mean bottom stresses increased the predicted setup by 16% on average for runs with roughness. As a result, setup on the reef flat was comparable (7% mean difference) between corresponding rough and smooth runs. These findings are used to assess prior results from numerical modeling studies of reefs and also to discuss the broader implications for how large roughness influences setup dynamics in the nearshore zone.

1. Introduction

Bottom roughness contributes to frictional wave dissipation and time-averaged (mean) bottom stresses, which modify surfzone force balances and resulting wave setup and wave-driven circulation (Longuet-Higgins 1970, 2005; Dean and Bender 2006; Lowe et al. 2009a). As a result, the large roughness features [O(0.1–1) m] typical of coral reefs can substantially influence a wide range of physical dynamics and dependent processes both physical (e.g., coastal inundation and sediment transport) and biological (e.g., larval and nutrient transport and dispersal; Roberts et al. 1975; Monismith 2007; Lowe et al. 2010; Lowe and Falter 2015). Coral reefs are subject to a range of stressors (e.g., climate-induced coral bleaching; eutrophication), which can ultimately reduce physical roughness through loss of coral cover (Alvarez-Filip et al. 2009) and in turn modify bottom stresses and alter reef hydrodynamics (Sheppard et al. 2005; Baldock et al. 2014; Quataert et al. 2015). In this paper, we specifically investigate how the presence of bottom roughness modifies wave setup dynamics.

Wave setup (the mean increase in water level due to wave breaking) along with tides and storm surge are the primary mechanisms controlling the water level at

Corresponding author address: Mark L. Buckley, School of Earth and Environment, University of Western Australia, Crawley WA 6009, Australia.
E-mail: mark.buckley@uwa.edu.au

DOI: 10.1175/JPO-D-15-0148.1

shorelines. Roughness affects setup through its contribution to the wave-averaged cross-shore momentum balance. For an alongshore uniform reef with normally incident waves, the wave-averaged and depth-integrated momentum equation in the cross-shore direction (x coordinate positive shoreward) can be expressed as (see Buckley et al. 2015)

$$\underbrace{\frac{\partial(S_{xx}+R_{xx})}{\partial x}}_{\text{radiation stress gradient}} + \underbrace{\rho g h \frac{\partial \overline{\eta}}{\partial x}}_{\text{pressure gradient}} + \underbrace{\overline{\tau}_b}_{\text{time-averaged bottom stress}} = 0, \quad (1)$$

where the overbars denote time averaging over many wave periods, S_{xx} is the cross-shore component of the wave radiation stress tensor (Longuet-Higgins and Stewart 1964), R_{xx} is the wave roller contribution to radiation stress (Svendsen 1984), ρ is the density, g is the gravitational acceleration, h_0 is the still water depth, $\overline{\eta}$ is the time-averaged deviation of the free surface η from h_0, $h = h_0 + \overline{\eta}$ is the total water depth, and $\overline{\tau}_b$ is the mean bottom stress (see summary of notation in Table 1).

Equation (1) describes the balance between the cross-shore components of the radiation stress and pressure gradients and the mean bottom stress. The radiation stress gradient term results from cross-shore gradients in potential and kinetic energy (e.g., due to wave shoaling and breaking; Buckley et al. 2015). In linear and other nonbreaking wave theories (e.g., cnoidal; Svendsen 2006, p. 420), both potential and kinetic energy are equal, allowing radiation stresses to be calculated with wave energy taken as twice the potential energy (e.g., Dean and Dalrymple 1991; Dean and Bender 2006). However, for breaking waves there is an additional source of kinetic energy (and radiation stress) from the wave roller traveling with the breaking wave (Duncan 1981; Svendsen 1984). The pressure gradient term results from cross-shore gradients in setdown and setup. The mean bottom stress $\overline{\tau}_b$ is generated by the interaction of the combined wave–current velocity field with bottom roughness and is commonly modeled using a quadratic drag law as (e.g., Grant and Madsen 1979; Feddersen et al. 2000; Mei et al. 2005)

$$\overline{\tau}_b = \rho C_d \overline{|u_b| u_b}, \quad (2)$$

where C_d is an empirical bulk bottom drag coefficient, and u_b is the instantaneous cross-shore free-stream velocity above the bottom roughness. Buckley et al. (2015) include a second-order term in their $\overline{\tau}_b$ formulation to account for the bottom slope; however, it is omitted here as it negligibly modifies $\overline{\tau}_b$ [proportional to $\sqrt{1+(\partial h_0/\partial x)^2}$], is small relative to all other terms in Eq. (1), and does not alter our results or conclusions.

Over smooth bottoms, Eq. (1) reduces to a balance between the radiation stress and pressure gradient terms (e.g., Bowen et al. 1968; Stive and Wind 1982; Buckley et al. 2015). However, in the presence of roughness the momentum balance is altered in two primary ways: 1) by increasing frictional wave dissipation, which in turn modifies radiation stress gradients and 2) by increasing the magnitude of $\overline{\tau}_b$ (Longuet-Higgins 2005; Dean and Bender 2006). Rates of frictional wave dissipation on coral reefs are commonly found to be at least one order of magnitude larger than is typical over smooth bottoms (Lowe et al. 2009b; Huang et al. 2012; Monismith et al. 2013, 2015). Lowe et al. (2009a) and Quataert et al. (2015) suggest that frictional wave dissipation offshore of the breakpoint may reduce setup on reefs. However, in part because of the difficulties in obtaining detailed surfzone measurements on coral reefs, the effects of these high frictional wave dissipation rates on setup dynamics have not yet been rigorously investigated experimentally.

The presence of a mean bottom stress $\overline{\tau}_b$ can contribute to either reducing or enhancing setup, depending on the sign of the velocity term in Eq. (2) (Dean and Bender 2006). Like frictional wave dissipation, $\overline{\tau}_b$ is commonly reported to be an order of magnitude larger on reefs than smooth bottoms under the same flow conditions (Lowe et al. 2009a; Rosman and Hench 2011). Numerical studies have predicted a significant portion of the total setup over fringing coral reefs (i.e., those fronting a coastline) is due to $\overline{\tau}_b$ generated by offshore-directed, near-bottom velocities (i.e., undertow) interacting with roughness (e.g., Franklin et al. 2013; Quataert et al. 2015). In contrast, Dean and Bender (2006) predicted that setup can theoretically be reduced when nonlinear wave orbital velocities interact with large roughness in the absence of any mean current.

In this study, we quantify the effect of large bottom roughness on setup dynamics using a high-resolution laboratory dataset. Experiments were conducted in a 55-m-long flume (1:36 scale) with a 1:5 reef slope leading to a wide shallow reef flat and sloping beach. The effect of roughness on setup was assessed by evaluating the cross-shore momentum balance from observations collected at 17 locations along the flume. Buckley et al. (2015) detail the cross-shore dynamics from the same flume, reef geometry, and wave conditions using a smooth bottom. In the present study, the 16 offshore wave heights and still water level conditions of Buckley et al. (2015) were repeated with the addition of a staggered array of cubes affixed to the reef slope and reef flat, which mimicked the typical bulk frictional wave dissipation characteristics of a coral reef. In this analysis, we specifically focus on how the introduction of the bottom roughness alters the wave dynamics and resulting setup profile.

TABLE 1. Notation.

Symbol	Definition	Unit
A_u, S_u	Velocity asymmetry A_u and velocity skewness S_u	—
β_D	Wave roller dissipation coefficient	—
C_d	Bulk bottom drag coefficient	—
$C_{\eta\eta}$	Wave power spectral density	$m^2\,Hz^{-1}$
C	Wave celerity	$m\,s^{-1}$
c_g	Wave group velocity	$m\,s^{-1}$
D_{br}	Wave energy dissipation due to breaking	$J\,m^{-2}\,s^{-1}$
D_{fric}	Wave energy dissipation due to roughness	$J\,m^{-2}\,s^{-1}$
η	Free-surface deviation from h_0	m
$\overline{\eta}$	Time-averaged η (e.g., wave setup or setdown)	m
$\overline{\eta}_{pred}$	Predicted $\overline{\eta}$ following Eq. (15)	m
$\overline{\eta}_r$	Time-averaged η on the reef flat	m
$\Delta\overline{\eta}$	Difference between maximum setdown and $\overline{\eta}_r$	m
E	Wave energy	$J\,m^{-2}$
E_r	Kinetic energy of the roller	$J\,m^{-2}$
F, F^+	Wave energy flux for the total and shoreward component, respectively	$J\,m^{-1}\,s^{-1}$
f	Frequency	s^{-1}
f_p	Peak wave frequency	s^{-1}
f_w	Wave bottom drag coefficient	—
g	Acceleration due to gravity	$m\,s^{-2}$
k	Wave number	radians m^{-1}
H_{rms}	Rms wave height	m
$H_{rms,0}$	Deep-water rms wave height	m
h	Total water depth	m
h_0	Local still water depth	m
$h_{0,r}$	Still water depth on the reef flat	m
λ_f	Frontal area of roughness elements per unit plan area	—
λ_p	Plane area of roughness elements per unit plan area	—
l_h, l_v	Horizontal l_h and vertical l_v dimensions of roughness elements	m
M_w	Wave mass flux	$kg\,m^{-1}\,s^{-1}$
M_r	Wave roller mass flux	$kg\,m^{-1}\,s^{-1}$
N	Number of roughness elements per unit plan area	m^{-2}
Ψ	Periodic forcing function	—
ρ	Density of water	$kg\,m^{-3}$
R_{xx}	Cross-shore component of the wave roller radiation stress	$N\,m^{-1}$
S_{xx}	Cross-shore component of the wave radiation stress tensor	$N\,m^{-1}$
$\Delta(S_{xx} + R_{xx})$	Cross-shore-integrated radiation stress gradient	$N\,m^{-1}$
σ_u	Standard deviation of u_b'	$m\,s^{-1}$
T_p	Peak wave period	s
$\overline{\tau}_b$	Time-averaged (mean) bottom stress	$N\,m^{-2}$
$\overline{\tau}_t$	Time-averaged shear stress at the boundary of the wave and the roller	$N\,m^{-2}$
U_b	Cross-shore time-averaged near-bottom velocity	$m\,s^{-1}$
u	Cross-shore instantaneous velocity	$m\,s^{-1}$
u_b	Cross-shore instantaneous near-bottom velocity	$m\,s^{-1}$
u_b'	Cross-shore instantaneous near-bottom wave velocity	$m\,s^{-1}$
ω	Wave angular frequency	radians s^{-1}

While this study is specifically motivated by how roughness modifies setup across reefs, our results are also broadly relevant to understanding how setup can be modified in other coastal systems having large roughness (e.g., as formed by aquatic vegetation, coarse sediment, bedforms, and karst topography).

2. Methods

a. Experimental setup

Experiments were performed in a 55-m-long wave flume (Eastern Scheldt flume) at Deltares, the Netherlands (Fig. 1). A 1:36 geometric-scale fringing reef profile was constructed from marine plywood with a 1:5 reef slope, a 14-m horizontal reef flat [500 m in field (prototype) scale], and a 1:12 beach (Fig. 1). The bathymetric characteristics of this reef fall within a typical range for fringing coral reefs (see Buckley et al. 2015). There were 2 sets of 16 runs conducted with varying still water depths on the reef flat $h_{0,r}$ and offshore wave conditions (Table 2). The first set of runs, detailed by Buckley et al. (2015), used a smooth bottom to minimize the role of bottom roughness on wave transformation and setup dynamics. In the second set of runs, bottom roughness was introduced using a staggered array of 1.8-cm (65 cm in field scale) concrete cubes affixed to the plywood bottom on the reef slope and reef flat (Fig. 2). This idealized array of roughness elements was designed to replicate the typical bulk frictional wave dissipation characteristics of reefs (Lowe et al. 2005b), while still being simple enough to have predictable hydrodynamic properties and be described with relatively few geometric variables. Analogous staggered arrays of roughness elements have been used to study flow through a variety of "canopies" (or "roughness sublayers"), including buildings (Macdonald 2000; Belcher et al. 2003), aquatic vegetation (Nepf and Vivoni 2000), and coral reefs (Chamberlain and Graus 1975; Lowe et al. 2005a, 2008; Zeller et al. 2015). The geometric properties of the cube array are defined by the horizontal and vertical dimensions of roughness elements l_h and l_v, respectively, and the density of roughness elements N (i.e., the number of roughness elements per unit plan area). From these variables, two nondimensional parameters are defined:

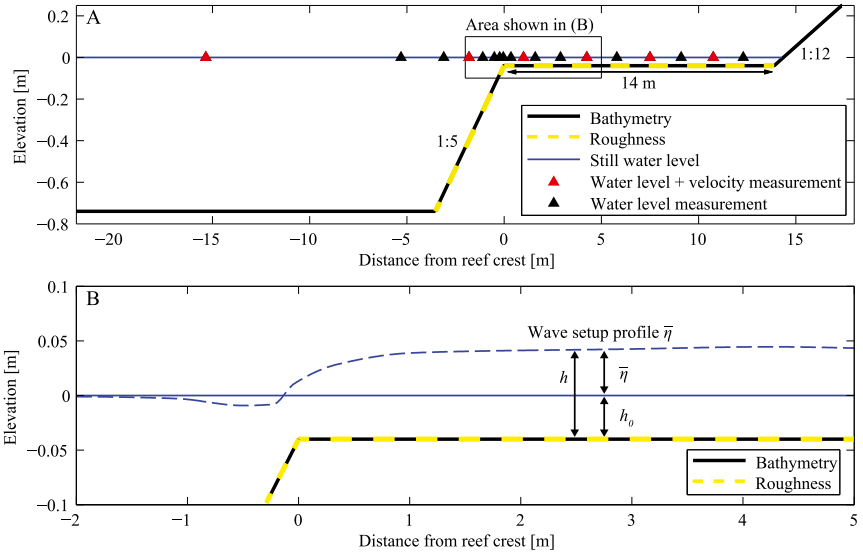

FIG. 1. (a) Schematic of the fringing reef showing the reef slope (1:5), reef flat length (14 m; ~500-m field scale), beach slope (1:12), and instrument locations. Sections of the bathymetry (reef slope and reef flat) highlighted in dashed yellow were affixed with roughness elements as shown in Fig. 2. (b) An example of the wave setup profile ($\overline{\eta}$) in the vicinity of the reef crest for run 4, defining the still water depth h_0 and the total water depth h.

$$\lambda_f \equiv l_h l_v N, \quad \text{and}$$
$$\lambda_p \equiv l_h l_h N, \tag{3}$$

where λ_f is the frontal area of roughness elements per unit plan area, and λ_p is the plan area of roughness elements per unit plan area. For the array of cubes used in this study, $N = 400\,\text{m}^{-2}$, $l_h = l_v = 1.8\,\text{cm}$, and $\lambda_f = \lambda_p = 0.13$ (Fig. 2), which is smaller than $\lambda_f = 0.42 - 6.31$ and comparable to $\lambda_p = 0.02 - 0.38$ reported for branched reef corals by Lowe et al. (2005a). We note that the presence of the solid roughness elements can modify the total water depth. Defining the total water depth h as the fluid volume in the water column divided by the plan area yields

$$h = h_0 + \overline{\eta} - \lambda_p l_v, \tag{4}$$

TABLE 2. Simulated wave and water level conditions, including the deep-water rms wave height $H_{\text{rms},0}$, peak period T_p, still water depth on the reef flat $h_{0,r}$, deep-water wave steepness $H_{\text{rms},0}/L_0$, and deep-water surf similarity parameter ξ_0. Parameter values are given for both the laboratory scale (i.e., 1:36 geometric scaling and 1: $\sqrt{36}$ scaling of time) and the equivalent field scale.

	Laboratory scale			Field scale				
Run	$H_{\text{rms},0}$ (m)	T_p (s)	$h_{0,r}$ (m)	$H_{\text{rms},0}$ (m)	T_p (s)	$h_{0,r}$ (m)	$H_{\text{rms},0}/L_0$ (—)	ξ_0 (—)
1	0.03	2.26	0.04	1.1	13.6	1.4	0.004	3.3
2	0.06	2.26	0.04	2.2	13.6	1.4	0.007	2.4
3	0.09	2.26	0.04	3.2	13.6	1.4	0.011	1.9
4	0.12	2.26	0.04	4.3	13.6	1.4	0.015	1.7
5	0.14	2.26	0.04	5.0	13.6	1.4	0.018	1.5
6	0.17	2.26	0.04	6.1	13.6	1.4	0.021	1.4
7	0.06	1.31	0.04	2.2	7.9	1.4	0.021	1.4
8	0.06	3.20	0.04	2.2	19.2	1.4	0.004	3.4
9	0.06	2.26	0.00	2.2	13.6	0.0	0.009	2.2
10	0.06	2.26	0.02	2.2	13.6	0.7	0.009	2.2
11	0.06	2.26	0.06	2.2	13.6	2.2	0.008	2.3
12	0.06	2.26	0.09	2.2	13.6	3.2	0.008	2.3
13	0.12	2.26	0.00	4.3	13.6	0.0	0.015	1.7
14	0.12	2.26	0.02	4.3	13.6	0.7	0.015	1.7
15	0.12	2.26	0.06	4.3	13.6	2.2	0.015	1.7
16	0.12	2.26	0.09	4.3	13.6	3.2	0.015	1.6

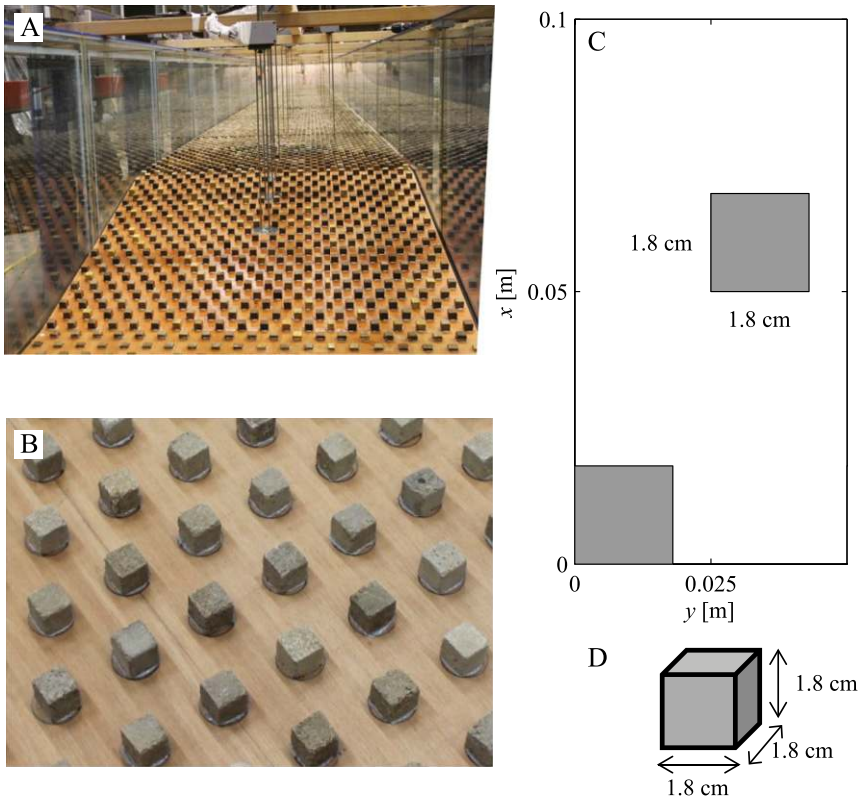

FIG. 2. (a) View of the dry flume with roughness elements looking shoreward from offshore of the reef slope. (b) Roughness elements used were (d) 1.8-cm concrete cubes affixed in the repeating staggered pattern shown in (c). This pattern gave $N = 400\,\mathrm{m}^{-2}$ cubes per unit plan area, with 7000 cubes in total covering the reef slope and flat.

where $h_0 + \overline{\eta}$ is the total water depth over a smooth bottom, and $\lambda_p l_v = 0.002\,\mathrm{m}$ is a correction due to the solid volume occupied by the roughness elements. However, this depth correction is less than 6% of the observed $h_0 + \overline{\eta}$, even on the shallow reef flat for cases where h_0 was lowest.

Irregular waves with a TMA spectrum (Bouws et al. 1985) were generated with a piston-type wave maker with second-order wave generation and active reflection compensation (van Dongeren et al. 2002). Water levels (17 locations with resistance-type gauges) and horizontal velocities (six locations with electromagnetic current meters) were measured synchronously at 40 Hz, with the highest density of measurements in the surfzone region near the reef crest at $x = 0\,\mathrm{m}$ (Fig. 1). On the reef flat and reef slope, instruments were recessed into the bed to sample in the shallow depths (Eslami Arab et al. 2012). At these locations, velocities were sampled over a volume extending from 2 to 2.5 cm above the bottom (the center of the volume was located at $z = -h_0 + 0.0225\,\mathrm{m}$, where z is the vertical coordinate positive upward from h_0). At other offshore locations, velocities were sampled at approximately the middle of the water column.

b. Calculation of radiation stresses

The methods used to evaluate both the wave (S_{xx}) and wave roller (R_{xx}) contributions to radiation stress are described in detail in Buckley et al. (2015) and briefly recounted here. Wave spectra $C_{\eta\eta}$ were computed using Welch's modified periodogram with a Hanning window and a segment length of 2^{14} samples (~410 s; 41 min in field scale). From $C_{\eta\eta}$, the wave energy flux F was evaluated as

$$F = \rho g \int c_g C_{\eta\eta}\, df. \tag{5}$$

The wave energy flux was separated into a component F_{SS} from sea swell (SS) waves and a component F_{IG} from infragravity (IG) waves. The SS band was defined as $f \geq f_p/2$ and the IG band was defined as $0.025 \leq f < f_p/2$, where f_p is the peak forcing frequency of each wave case (Table 2). Following Buckley et al. (2015), the collocated synchronous water level and velocity measurements were used to estimate the shoreward-propagating components of wave energy flux (F^+_{SS} and F^+_{IG}) from which S_{xx} was evaluated at instrument locations as

$$S_{xx} = \frac{F^{+}_{SS}}{c_g(f_{SS,mean})}\left[2\frac{c_g(f_{SS,mean})}{c(f_{SS,mean})} - \frac{1}{2}\right] + \frac{F^{+}_{IG}}{c_g(f_{IG,mean})}\left[2\frac{c_g(f_{IG,mean})}{c(f_{IG,mean})} - \frac{1}{2}\right], \quad (6)$$

where $f_{SS,mean}$ and $f_{IG,mean}$ are defined as the mean frequencies for the SS and IG waves, respectively.

As discussed in Buckley et al. (2015), wave rollers contribute an additional source of radiation stress R_{xx} in the surfzone as (Svendsen 1984)

$$R_{xx} = 2E_r, \quad (7)$$

where E_r is the kinetic energy of the wave roller, modeled using an approximate energy balance following Stive and De Vriend (1994):

$$\frac{\partial}{\partial x}(2E_r c) = D_{br} - \overline{\tau}_t c. \quad (8)$$

Here, D_{br} is the wave breaking dissipation rate, and $\overline{\tau}_t$ is the mean shear stress at the boundary between the turbulent roller and the underlying organized wave motion. Following Buckley et al. (2015), $\overline{\tau}_t$ is modeled according to Dally and Brown (1995) with the wave roller dissipation coefficient $\beta_D = 0.019$ found to be optimum by Buckley et al. (2015) for the smooth runs. Wave breaking dissipation was isolated from the total dissipation as

$$D_{br} = \underbrace{-\frac{\partial(F^{+}_{SS} + F^{+}_{IG})}{\partial x}}_{\text{total dissipation}} - \underbrace{D_{fric}}_{\text{roughness dissipation}}, \quad (9)$$

where D_{fric} is the frictional wave dissipation over the immovable bed, modeled as (Jonsson 1966)

$$D_{fric} = \frac{1}{2}\rho f_w \overline{|u_b^{\prime 3}|}, \quad (10)$$

where f_w is the wave friction factor (detailed in section 3a), and u_b' is the wave component of u_b (see section 3c).

The methods by which radiation stresses were estimated account for nonlinear wave shape through a spectral representation of the wave field (see Buckley et al. 2015). Conservative nonlinear interactions between sea swell and infragravity waves are inherently accounted for, as Eq. (1) is averaged over both sea swell and infragravity wave frequencies. All waves are assumed to be free and progressive despite that a portion of the shoreward-propagating infragravity energy offshore of the breakpoint is likely bound to the sea swell wave groups (Longuet-Higgins and Stewart 1962, 1964). However, because of the low proportion (less than 4%) of infragravity wave energy offshore of the breakpoint (Buckley et al. 2015), the assumption of free versus bound infragravity waves has negligible effect on the calculation of S_{xx} and hence wave setup. Likewise, nonlinear interactions between sea swell and infragravity waves that can modify the infragravity wave energy balance (Henderson et al. 2006; Pequignet et al. 2014) are calculated to be less than 5% of the combined sea swell and infragravity wave energy flux and therefore are negligible in this evaluation of wave setup dynamics.

c. Evaluation of velocities

Although velocities were measured at six locations (Fig. 1), higher spatial resolution was required to determine the mean bottom stress term in Eq. (1) across the reef profile. The methods used to predict velocities are detailed below and comparisons of the predicted and observed velocities are included in section 3d. The instantaneous velocity u_b was composed of a steady (current) component U_b and an unsteady (wave) component u_b':

$$u_b = U_b + u_b', \quad (11)$$

where the subscript b denotes the free-stream velocity at the top of the roughness elements ($z = -h_0 + l_v$). The steady component U_b was approximated as the time- and depth-averaged Eulerian velocity (Apotsos et al. 2007; Lentz et al. 2008). For all cases considered here, the system was in steady state when averaged over many wave cycles (i.e., $\overline{\partial/\partial t} = 0$) and the shoreline was impermeable, such that the time-averaged and depth-integrated Lagrangian mass flux was zero (e.g., Mei et al. 2005). This allowed U_b to be approximated from local continuity as the offshore-directed velocity necessary to balance the onshore-directed mass flux above the mean water level due to finite-amplitude nonbreaking waves and wave rollers (Faria et al. 2000; Apotsos et al. 2007; Lentz et al. 2008):

$$U_b = -\underbrace{\frac{M_w}{\rho h}}_{\substack{\text{wave}\\ \text{mass flux}}} - \underbrace{\frac{M_r}{\rho h}}_{\substack{\text{wave roller}\\ \text{mass flux}}}, \quad (12)$$

where $M_w = E/c$ (based on the wave energy density $E = F/c_g$) and $M_r = 2E_R/c$ are the depth-integrated and time-averaged Eulerian mass fluxes due to the nonbreaking waves and wave rollers, respectively.

The wave velocity u_b' for the combined sea swell and infragravity wave field was approximated using a time series of nonlinear waves based on Ruessink et al. (2012):

$$u_b' = \underbrace{\frac{H_{\text{rms}}\omega_{\text{mean}}\cosh(k_{\text{mean}}l_v)}{2\sinh(k_{\text{mean}}h)}}_{\text{velocity amplitude}} \underbrace{\Psi(t, f_{\text{mean}}, A_u, S_u)}_{\text{periodic forcing function}}, \quad (13)$$

where H_{rms} is the combined sea swell and infragravity root-mean-square (rms) wave height, f_{mean} is the mean frequency, $\omega_{\text{mean}} = 2\pi f_{\text{mean}}$ is the mean angular frequency, and k_{mean} is the mean wavenumber approximated from linear wave theory. The first term represents the linear wave theory–derived wave velocity amplitude for free progressive waves, and the second term is a normalized periodic forcing function Ψ that generates a time-dependent t signal of frequency f_{mean} with velocity asymmetry A_u and velocity skewness S_u [see Ruessink et al. (2012) for the mathematical form and evaluation of Ψ]. Velocity skewness S_u and asymmetry A_u are measures of the asymmetry of the velocity signal about the horizontal and vertical axes, respectively, and thus influence the mean bottom stress via the velocity term in Eq. (2). Velocity skewness is defined as

$$S_u \equiv \frac{\overline{u_b'^3}}{\sigma_u^3}, \quad (14)$$

where σ_u is the standard deviation of u_b'. Velocity asymmetry A_u is defined similarly to Eq. (14) but with u_b' replaced by its Hilbert transform (Ruessink et al. 2012). The velocity nonlinearity parameters S_u and A_u were evaluated from velocity time series where available and by using the linear wave theory transfer function (e.g., Guza and Thornton 1980) to first convert water level time series to predicted velocity time series for sites with only water level measurements (Fig. 1).

d. Evaluation of the mean momentum equation

Terms in the mean momentum equation were evaluated from observations of $S_u, A_u, \overline{\eta}, f_{\text{mean}}, f_{\text{SS,mean}}, f_{\text{IG,mean}}$, F_{SS}^+, and F_{IG}^+, which were interpolated using a shape-preserving piecewise cubic algorithm onto a uniform 0.01-m grid extending from offshore ($x = -4.0$ m) to near the shoreline ($x = 14$ m; Buckley et al. 2015). Over this domain, the cross-shore spacing between wave gauges varied from 0.19 m (~1/40 of the incident wavelength) in the surfzone to 1.7 m (~1/4 of the incident wavelength) on the reef flat (Fig. 1). At each grid location, the mean bottom stress was evaluated from the interpolated observations via Eq. (2), where U_b and u_b' were evaluated via Eqs. (12) and (13), respectively. The radiation stresses S_{xx} and R_{xx} were evaluated from the interpolated observations via Eqs. (6) and (7), respectively. Cross-shore pressure and radiation stress gradient terms were computed using central differencing. The contributions of radiation stress gradients and mean bottom stresses to the setup response were evaluated by "predicting" setup across the reef, via Eq. (1) as (e.g., Raubenheimer et al. 2001; Buckley et al. 2015)

$$\overline{\eta}_{\text{pred}} = -\int_{x_0}^{x} \frac{1}{\rho g h}\left[\frac{\partial(S_{xx} + R_{xx})}{\partial x} + \overline{\tau}_b\right] dx + \overline{\eta}(x_0), \quad (15)$$

where the integration was initialized at a seaward deep-water boundary x_0 ($x_0 = -4$ m in Fig. 1), where we assume $\overline{\eta}(x_0) = 0$ and was evaluated iteratively using trapezoidal integration.

e. Uncertainty estimates

Using the same resistance-type water level gauges, Buckley et al. (2015) estimated uncertainties of ±0.5% outside of the surfzone and ±1.5% within the surfzone of the measured range for time-averaged water levels. Likewise, uncertainties were estimated to be ±2% outside of the surfzone and ±7% inside the surfzone for parameters proportional to wave height squared (e.g., wave energy and radiation stresses). The larger uncertainty values within the surfzone are due to aeration of the water column during wave breaking (Stive and Wind 1982). The effect of these uncertainties on the cross-shore integration of Eqs. (1) and (15) was assessed by performing 100 Monte Carlo simulations, where uncertainties were modeled as having zero-mean Gaussian random distributions with a standard deviation equivalent to the uncertainty.

3. Results

a. Wave transformation and setup dynamics

Buckley et al. (2015) describe the dynamics of wave transformation and resulting setdown and setup for the smooth runs; here, we specifically focus on the dynamical differences due to the inclusion of bottom roughness. Following Buckley et al. (2015), we first outline the results from a moderate case (run 4), which had a relatively large (0.12 m; 4.3 m in field scale) deep-water wave height and an intermediate (0.04 m; 1.4 m in field scale) still water depth (Table 2). Compared to run 4 over the smooth bottom, including roughness led to a slightly reduced wave height at the breakpoint and across the reef flat (Fig. 3a). This pattern was consistent across all runs (Fig. 4a). The wave height to water depth ratios on the reef flat were also lower for runs with roughness (Fig. 4b) because of increased frictional wave dissipation on the reef flat. From the dimensions and spacing of the roughness elements and the wave forcing, the wave friction factor predicted using the canopy flow equations of Lowe et al. (2007) is $f_w = 0.16$. Using Eqs. (9) and (10) along with the wave energy dissipation rate $[\partial(F_{\text{SS}}^+ + F_{\text{IG}}^+)/\partial x]$ measured on the reef flat shoreward of the surfzone where

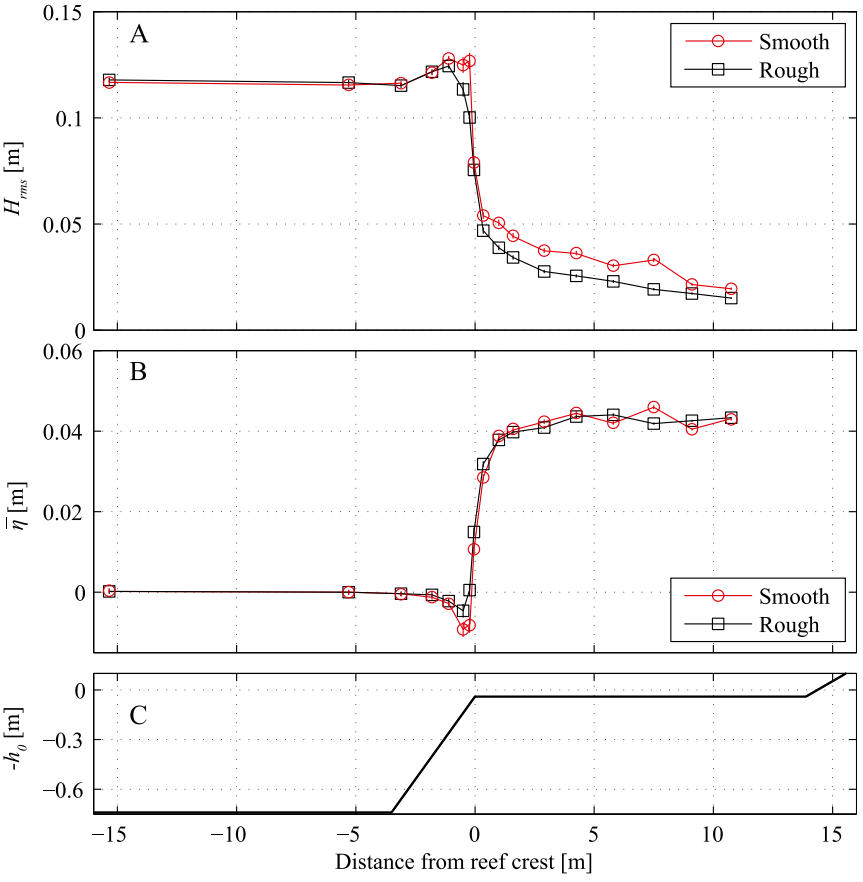

FIG. 3. (a) Wave height $H_{\rm rms}$ and (b) wave setup $\overline{\eta}$ across (c) the fringing reef profile for run 4 both including (rough) and without (smooth) roughness. Vertical error bars show the uncertainties due to instrument accuracy and are negligible here (see section 2e).

wave breaking was absent ($x > 8$m), we find a comparable $f_w = 0.2$ for all runs with roughness. The value $f_w = 0.2$ is also within the typical range for many coral reefs, for example, $f_w = 0.15$ (Nelson 1996), $f_w = 0.22$ (Falter et al. 2004), and $f_w = 0.24$ (Lowe et al. 2005a).

Setup profiles for run 4 were similar between the rough and smooth runs (Fig. 3b); however, we note that there were differences near the reef crest ($x = 0$ m) and that setdown for the smooth run 4 was twice that of the rough run 4 (Fig. 3b). On average across all runs, setdown was 80% larger for the smooth runs than the rough runs (Fig. 5a). Of particular interest is setup on the reef flat, which was relatively constant for $x > 4$ m (Fig. 3b). As such, following Buckley et al. (2015), we define the representative setup on the reef flat $\overline{\eta}_r$ as the spatially averaged $\overline{\eta}$ between $x = 4$ and 10 m (Fig. 3b). Despite differences in the wave height profiles and $\overline{\eta}$ near the reef crest, run 4 $\overline{\eta}_r$ was identical ($\overline{\eta}_r = 0.043$ m) for both the rough and smooth runs (Fig. 3b). On average across all runs, there was only a 7% difference in $\overline{\eta}_r$ between rough and smooth runs (Fig. 5b). The total setup generated $\Delta\overline{\eta}$, defined as the difference between maximum setdown and $\overline{\eta}_r$, was larger in the smooth runs, with the exception of run 1, which had the smallest $\Delta\overline{\eta}$ (Fig. 5c).

b. *Evaluation of the mean bottom stress*

To relate the observations of $\overline{\eta}$ to the mean momentum balance, we first integrate Eq. (1) in the cross-shore direction:

$$\int_{x_0}^{x} \frac{\partial (S_{xx} + R_{xx})}{\partial x}\, dx + \int_{x_0}^{x} \rho g h \frac{\partial \overline{\eta}}{\partial x}\, dx + \int_{x_0}^{x} C_d \rho \overline{|u_b| u_b}\, dx = 0, \tag{16}$$

where the bounds of integration were taken from seaward of the breakpoint ($x_0 = -4$ m) to a point on the reef flat ($x = 4$ m) shoreward of the surfzone where $\overline{\eta}$ becomes relatively constant [i.e., $\overline{\eta}(x) \approx \overline{\eta}_r$]. We note that the cross-shore-integrated radiation stress gradient is only dependent on the endpoint values, allowing us to restate the term as $\Delta(S_{xx} + R_{xx})$. Buckley et al. (2015) found that for the smooth runs where $\overline{\tau}_b \approx 0$, Eq. (16) reduced to a

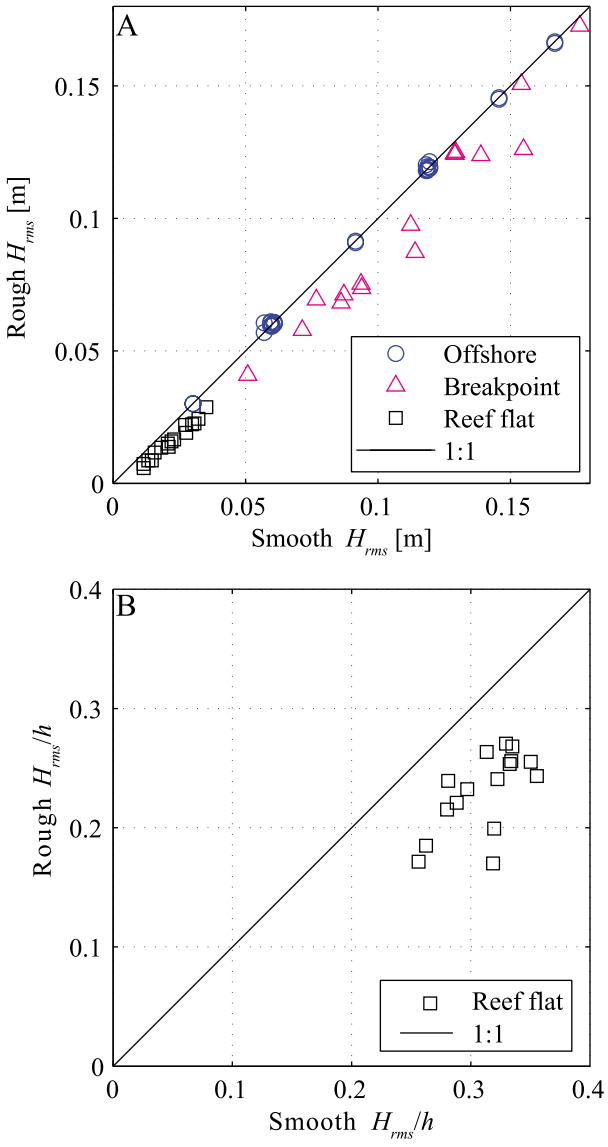

FIG. 4. (a) Comparison of the rms wave heights $H_{\rm rms}$ and (b) wave height to water depth ratios $H_{\rm rms}/h$ on the reef flat for runs including (rough) and without (smooth) roughness.

balance between the cross-shore-integrated pressure and radiation stress gradients (red circles approximately along the 1:1 line in Fig. 6). Conversely for runs with roughness, the cross-shore-integrated pressure gradient was typically larger than the cross-shore-integrated radiation stress gradient (black squares in Fig. 6). Assuming the momentum balance [Eq. (16)], these differences should be accounted for by the contribution of the cross-shore-integrated mean bottom stress term.

To evaluate the mean bottom stress term via Eq. (2) requires estimates of the bulk bottom drag coefficient C_d and the instantaneous free-stream near-bottom velocity u_b. The near-bottom velocity u_b was estimated as the sum of a mean current component and a nonlinear wave component [following Eq. (12) and (13), respectively]. The rms wave velocity was determined via linear wave theory based on the observed wave field. At locations where velocity was measured the estimated wave velocities agreed with the observations ($r^2 = 0.96$; slope = 1.01; Fig. 7a). As the waves and corresponding velocities demonstrated nonlinear characteristics (Fig. 8), velocity skewness S_u and asymmetry A_u were included via the periodic forcing function in Eq. (13). The mean current velocities predicted based on the wave and wave roller mass flux also compared well with observations ($r^2 = 0.89$; slope = 0.94; Fig. 7b). From Eq. (16), a representative C_d was estimated as the least squares slope between the sum of the cross-shore-integrated pressure and radiation stress gradients and the cross-shore-integrated velocity term from all runs including roughness (e.g., Feddersen and Guza 2003; Fig. 9). This yielded $C_d = 0.028$ ($r^2 = 0.7$), which is an order of magnitude larger than that typically found over smooth bottoms $O(0.001)$ (e.g., Faria et al. 1998) but within the range from 0.02 to 0.1 reported for coral reefs (Lowe et al. 2009a; Rosman and Hench 2011).

c. Predicted wave setup

The estimated radiation stresses and mean bottom stresses (computed using $C_d = 0.028$ and u_b) were used to predict the cross-shore setup profiles via Eq. (15) and compared with the observed setup (Figs. 10, 11). For run 4 with roughness (Fig. 10), neglecting $\overline{\tau}_b$ ($C_d = 0$) resulted in a 16% underprediction of $\overline{\eta}_r$, which was reduced to only 2% when $\overline{\tau}_b$ ($C_d = 0.028$) was included (Fig. 10). Across all runs with roughness, $\overline{\eta}_r$ was underpredicted by 18% on average when $\overline{\tau}_b$ was neglected (Fig. 11) compared to 7% when $\overline{\tau}_b$ was included with $C_d = 0.028$ (Fig. 11). Neglecting infragravity waves decreased the predicted $\overline{\eta}_r$ by only 3% on average.

d. Bottom stress decomposition

Thus far, $\overline{\tau}_b$ has been evaluated via Eq. (2) using velocity estimates that include contributions from near-bottom currents [Eq. (12)], wave velocities [Eq. (13)], and the interactions between the two. However, many analytical and numerical models estimate u_b in differing ways and generally only resolve certain contributions to the true velocity field, as summarized in Table 3. Figure 12 shows a comparison of $\overline{|u_b|u_b}$ calculated using the observed velocity from locations with current meters on the reef flat (Fig. 1) with $\overline{|u_b|}u_b$ predicted via Eqs. (12) and (13) and with various individual contributions to u_b neglected (see Table 3). The full velocity estimate using Eqs. (12) and (13) (i.e., $u_b = U_b + u_b'$ with A_u and S_u calculated from observations) provides the best match

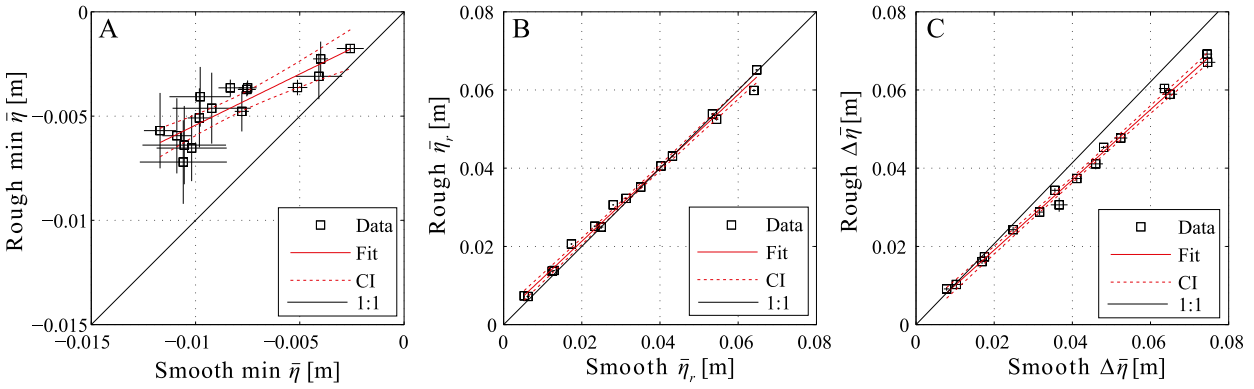

FIG. 5. (a) Comparison of maximum setdown, (b) setup on the reef flat $\overline{\eta}_r$, and (c) setup generation $\Delta\overline{\eta}$ for runs including (rough) and without (smooth) roughness. Solid red lines give the linear least squares trend lines (fit) and dashed red curves give the upper and lower bounds of the 95% confidence interval (CI) for the trend line. Vertical and horizontal error bars show the uncertainties due to instrument accuracy (see section 2e). Note the scale change between (a) and (b) and (c), which renders error bars in (b) and (c) less visible.

to the observed velocities (r^2 = 0.8 and slope = 0.98; Fig. 12). For the other methods in Table 3, the agreement between observed and predicted $\overline{|u_b|u_b}$ deteriorates as various velocity contributions are neglected (Fig. 12). As $\overline{|u_b|u_b}$ directly relates to the mean bottom stress, this demonstrates the sensitivity of $\overline{\tau}_b$ to which components of a combined wave–current velocity field are resolved (e.g., as are assumed within different classes on numerical models; Table 3).

Here, we repeat the analysis performed in Fig. 8 with the various implementations of u_b described in Table 3 (Fig. 13). This allows us to quantitatively assess how neglecting various contributions to u_b affect empirical estimates of the bulk bottom drag coefficient C_d that is the basis for predicting $\overline{\tau}_b$ (Fig. 13). The range of different classes of numerical models in Table 3 can thus be expected to reproduce $\overline{|u_b|u_b}$ with varying accuracies and bias (Fig. 12). For example, neglecting the role of unsteady wave velocities (u_b') results in a significant underprediction of $\overline{|u_b|u_b}$. Conversely, neglecting velocity nonlinearity (i.e., assuming $A_u = S_u = 0$) slightly overpredicts $\overline{|u_b|u_b}$ (Fig. 12). Local inaccuracies in the predicted $\overline{|u_b|u_b}$ can therefore result in both higher and lower predictions of the cross-shore-integrated $\overline{|u_b|u_b}$ term (Fig. 13), which thus requires adjusting C_d in order to balance the sum of the cross-shore-integrated pressure and radiation stress gradients per Eq. (16) (Fig. 13; Table 3). As a result, C_d estimates using these various approaches' range by nearly an order of magnitude (0.027 and 0.23) when applied to the identical dataset (Table 3). Neglecting both wave velocities and the wave roller (i.e., $u_b = U_b$ with $M_r = 0$) yielded the smallest estimate of $\overline{|u_b|u_b}$ (Fig. 12) and hence the largest C_d = 0.23 (a factor of 8 larger than C_d = 0.028; Fig. 13; Table 3). Neglecting A_u and S_u (i.e., $u_b = U_b + u_b'$ with $S_u = A_u = 0$) yielded the smallest C_d = 0.027 (albeit only 4% less than C_d = 0.028; Fig. 13; Table 3). These results highlight a possible nonphysical source of variability and uncertainty in C_d based on estimates from various field studies and numerical model applications to coral reefs with large bottom roughness [see Lowe et al. (2009a) and Rosman and Hench (2011) for a review of C_d values reported on coral reefs].

4. Discussion

The presence of bottom roughness influences wave setup through two primary mechanisms:

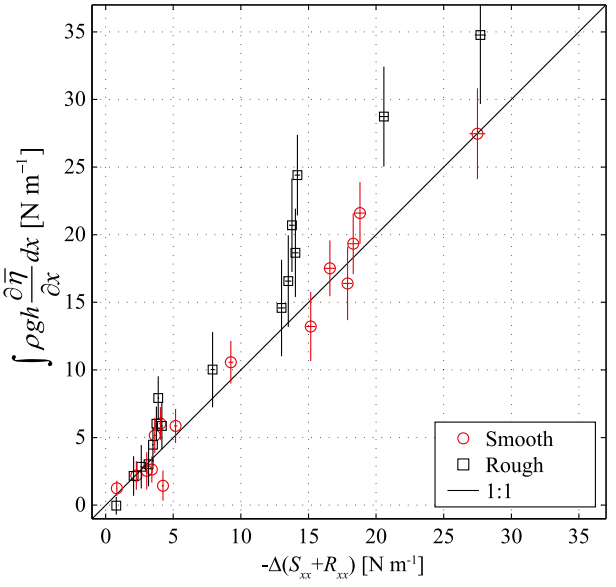

FIG. 6. Comparison of the cross-shore-integrated radiation stress [$-\Delta(S_{xx} + R_{xx})$] and pressure gradient terms for runs including (rough) and without (smooth) roughness. Vertical and horizontal (generally not visible) error bars show the uncertainties due to instrument accuracy (see section 2e).

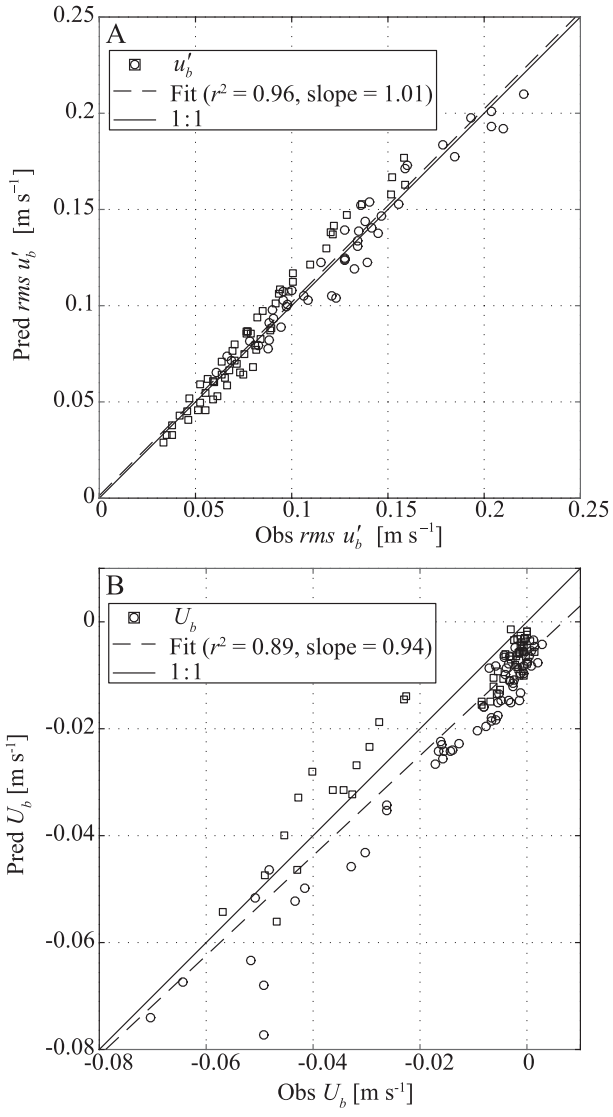

FIG. 7. Comparisons of the observed (obs) and predicted (pred) time-averaged (a) rms wave velocities u_b' and (b) mean velocities U_b. Data are shown for both smooth runs (open circles) and with roughness (open squares). Dashed lines give the linear least squares trend lines, while the solid line indicates 1:1.

1) the cross-shore distribution of wave energy is modified; and
2) mean bottom stresses are generated.

In mechanism 1, frictional wave dissipation results from the work done by bottom roughness resistance forces on wave velocities and is parameterized per Eq. (10) as being proportional to $\overline{|u_b'^3|}$ and f_w. In mechanism 2, mean bottom stress is generated by the time-averaged resistance forces exerted by the bottom roughness on the combined wave–current velocities and is parameterized per Eq. (2) as being proportional to $\overline{|u_b|u_b}$ and C_d. Both C_d and f_w are a function of the flow characteristics and the physical scale of bottom roughness (Nielsen 1992). However, over rough bottoms f_w is typically found to be an order of magnitude or larger than C_d [see Nielsen (1992) for a review]. For example, in this study we found $C_d = 0.028$ and $f_w = 0.2$ on average for runs that included roughness.

Through the first mechanism, we found that the inclusion of bottom roughness resulted in the frictional dissipation of wave energy seaward of the breakpoint (Figs. 3, 4, 10a). This redistribution of wave energy (Fig. 10a) resulted in an average 13% decrease in the H_{rms} at the breakpoint and an average 26% decrease in maximum radiation stresses ($S_{xx} + R_{xx}$) when comparing the rough runs to the smooth runs (shown for run 4 in Fig. 10b). As a result, despite the magnitude of the cross-shore-integrated radiation stress gradients being 9% larger on average when roughness was included (Fig. 6), $\overline{\eta}_r$ predicted from the radiation stress gradients (neglecting mean bottom stresses; $C_d = 0$) was on average 18% less for the rough runs compared to the smooth runs (Fig. 11). However, through the second mechanism, mean bottom stresses for the rough runs increased the predicted $\overline{\eta}_r$ by 16% on average compared to predictions neglecting mean bottom stresses (Fig. 11). Mechanisms 1 and 2 thus counteracted each another, and despite modifying the setdown and changing the partitioning of radiation stress gradients and mean bottom stresses, the roughness did not considerably alter the final values of setup on the reef flat, which differed less than 10% on average for corresponding rough and smooth runs (Figs. 3, 5).

Mechanisms 1 and 2 apply generally to nearshore systems governed by Eq. (1), including many relatively alongshore uniform reefs and beaches. However, in contrast to our experimental findings, numerical model predictions (Apotsos et al. 2007; Franklin et al. 2013) have suggested there can be appreciable increases in setup due to bottom roughness principally through mean bottom stresses.

By neglecting frictional wave dissipation in their phase-averaged wave transformation model (i.e., neglecting mechanism 1) and using a $C_d = 0.028$ in the surfzone to predict mean bottom stresses (hence the same C_d we found in our study), Apotsos et al. (2007) estimated that 30% of the setup response on a sandy beach was due to bottom roughness. Although frictional wave dissipation is commonly assumed to be small compared to wave breaking dissipation on sandy beaches (e.g., Guza and Thornton 1981), wave friction factors f_w typically are an order of magnitude larger than the drag coefficient C_d used to estimate bottom stresses. Thus, given the $C_d = 0.028$ used by Apotsos et al. (2007) to

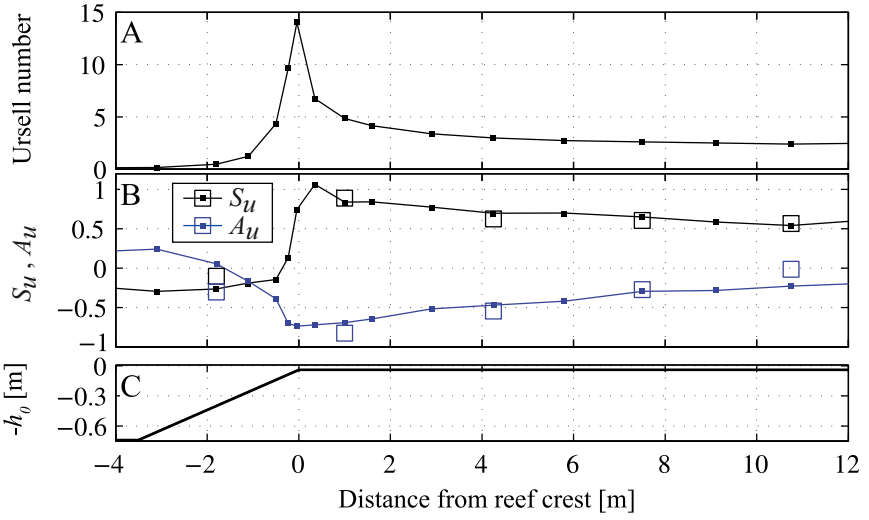

FIG. 8. (a) Ursell number (a measure of wave nonlinearity; Doering and Bowen 1995) and (b) velocity skewness S_u and asymmetry A_u are shown over (c) the bathymetric profile for runs including roughness. In (b), small filled squares and connecting lines are S_u and A_u approximated from water level time series, and large open squares are values calculated from the velocity time series.

predict mean bottom stresses, one would also expect a correspondingly large f_w to have resulted in modifications to the wave field in their study. In our experiments, if we neglected the frictional wave dissipation (mechanism 1) by using the smooth simulations but include mean bottom stresses with $C_d = 0.028$ (mechanism 2), an average 25% increase in setup is predicted via Eq. (15) across all runs, thus comparable to the 30% increase predicted by Apotsos et al. (2007). In another numerical study, Franklin et al. (2013) reported a ~20% increase in setup due to roughness across a fringing reef. They based their study on numerical simulations with a phase-resolving Reynolds-averaged Navier–Stokes (RANS) model of the smooth laboratory reef experiments of Demirbilek et al. (2007) and assessed how setup responded to increasing Nikuradse roughness coefficients between 0 and 0.05 m (corresponding to $C_d = 0$ to ~0.01). Inconsistent with our findings, they predicted that an increase in the roughness coefficient increased the mean bottom stress without resulting in any significant reduction in wave heights at the breakpoint (Franklin et al. 2013). This creates a dynamic similar to Apotsos et al. (2007), where wave forces are held relatively constant and mean bottom stresses are increased.

Ultimately, the accuracy of theoretical and numerical model predictions of setup over rough bottoms will be determined by both the representation of wave transformation (see Buckley et al. 2015) and the prediction of mechanisms 1 and 2. Although the RANS model used by Franklin et al. (2013) incorporates a more physically complete description of wave transformation and other dynamics compared to phase-averaged models, a single bulk bottom drag coefficient is applied within these models irrespective of type of flow (i.e., wave versus current). Such an approach does not account for the

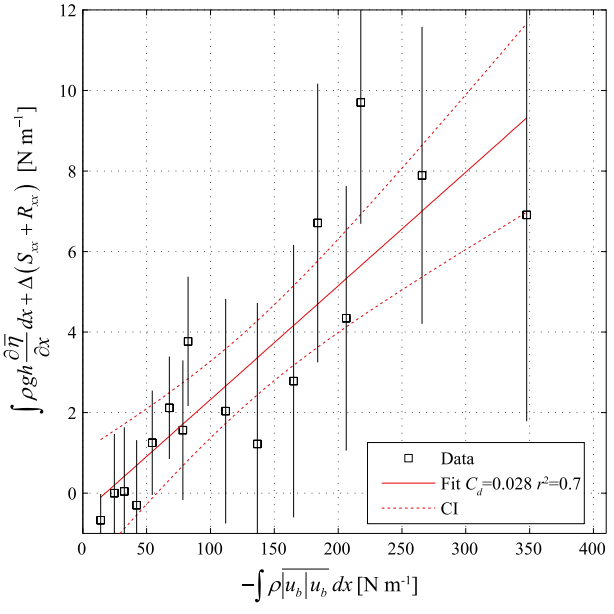

FIG. 9. Comparison of the cross-shore-integrated time-averaged velocity term with the sum of the cross-shore-integrated pressure and radiation stress gradient terms for runs including roughness. Per Eq. (16), the linear least squares trend line (fit; solid red lines) gives the estimated bulk bottom drag coefficient ($C_d = 0.028$) cross-shore averaged and averaged across all runs with roughness. The dashed red curves show the upper and lower bounds of the 95% CI for the trend line. Vertical error bars show the uncertainties due to instrument accuracy (see section 2e).

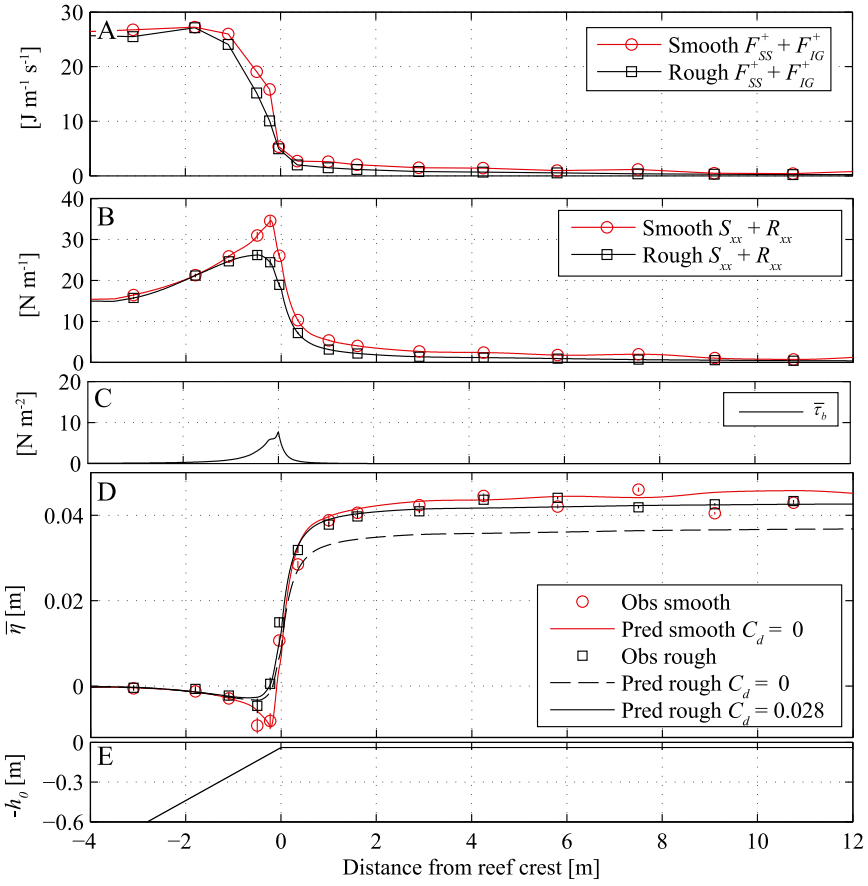

FIG. 10. (a) Shoreward wave energy flux from sea swell F_{SS}^{+} and infragravity F_{IG}^{+} waves, (b) radiation stresses $S_{xx} + R_{xx}$, and (c) mean bottom stresses $\overline{\tau}_b$ across (e) the fringing reef profile for run 4 including (rough) and without (smooth) roughness. (d) Radiation stress gradients and mean bottom stresses were used for predicted (pred) setup $\overline{\eta}$ via Eq. (15) and compared with observations (obs). For the smooth run, $\overline{\eta}$ was well predicted without $\overline{\tau}_b$ (i.e., $C_d = 0$). However, for the rough run $\overline{\eta}$ was underpredicted without $\overline{\tau}_b$ (i.e., $C_d = 0$) but was well predicted with the estimated $\overline{\tau}_b$ ($C_d = 0.028$).

known differences between f_w and C_d in the presence of roughness (Nielsen 1992). Alternatively, in coupled phase-averaged wave and flow models, f_w and C_d are often independently varied. This was done in a recent numerical study aimed at predicting the hydrodynamic impacts of climate change on coral reefs by Quataert et al. (2015) using the XBeach model (Van Dongeren et al. 2013). In agreement with the mechanisms 1 and 2 discussed above, Quataert et al. (2015) theoretically predicted decreasing setup with increasing f_w (mechanism 1) and increasing setup with increasing C_d (mechanism 2). However, Quataert et al. (2015) lacked data to validate their numerical predictions and a physical basis for how f_w and C_d should be related. These numerical studies highlight the need for a more precise method of modeling mechanisms 1 and 2 in both phase-resolving and phase-averaged numerical models.

Although not considered in traditional nearshore models (e.g., Franklin et al. 2013; Quataert et al. 2015), nor explicitly in either Eq. (2) or Eq. (10), it is the velocity terms $\overline{|u^3|}$ and $\overline{|u|u}$ within the roughness sublayer (or canopy; not above) that interact with roughness to generate wave dissipation and mean bottom stresses, respectively. For large roughness, previous studies have shown these velocities within the canopy are both reduced compared to those above and that the attenuation is frequency dependent, being most attenuated in a unidirectional flow (Lowe et al. 2005b; Luhar et al. 2010; Zeller et al. 2015). Traditionally, Eq. (2) and Eq. (10) are cast in terms of the velocities at the top of the roughness (e.g., Apotsos et al. 2007; Franklin et al. 2013; Quataert et al. 2015). As such, in addition to relating the local flow velocities to the resistance forces and the work done by resistance forces, respectively, C_d and f_w must also

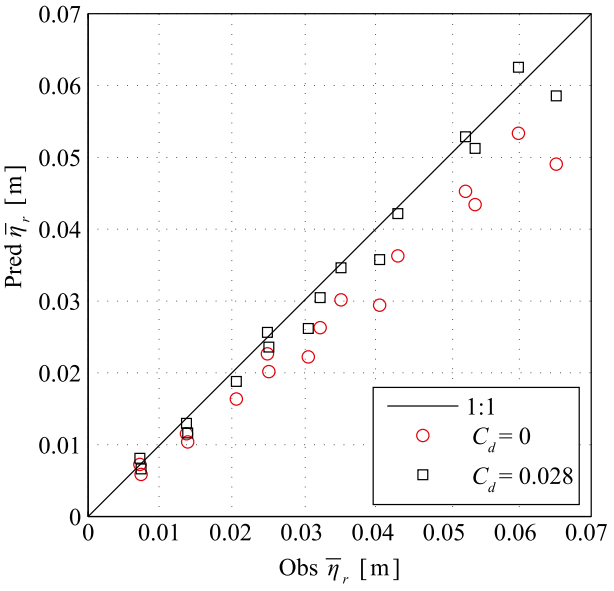

FIG. 11. Comparison of observed (obs) and predicted (pred) wave setup on the reef flat $\overline{\eta}_r$ for runs with roughness. Wave setup is predicted from observation of radiation stress gradients via Eq. (15) neglecting (red circles; $C_d = 0$) and including (black squares; $C_d = 0.028$) the predicted mean bottom stress.

account for the attenuation of velocities within the canopy that modify the velocities directly interacting with the roughness elements. The attenuation of velocities within canopies has previously been modeled by treating the canopy as a sublayer using a spatially and depth-averaged momentum equation (Nepf and Vivoni 2000; Lowe et al. 2005b; Zeller et al. 2015). Canopy flow models have been successfully used to predict the frequency-dependent dissipation of wave energy without the need to specify differing empirical coefficients for waves and currents (Lowe et al. 2007; Jadhav et al. 2013). Thus, implementing canopy flow dynamics into existing numerical models, such as those used by Franklin et al. (2013) and Quataert et al. (2015), should improve the representation of mechanisms 1 and 2 and allow for more accurate numerical predictions of setup under different bathymetric configurations, hydrodynamic conditions, and roughness characteristics.

While the present study specifically focuses on how bottom roughness influences setup over a representative fringing coral reef profile, the results are also expected to be broadly applicable to other nearshore systems with large roughness (e.g., due to vegetation, coarse sediment, and bedforms). The setup response to roughness will be determined by both the response of the radiation stress gradients (mechanism 1) and the mean bottom stress (mechanism 2). In many environments, as was the case here, the two mechanisms may cancel, resulting in no appreciable change in setup at the shoreline. However, in other environments the specific physical setting may result in one of the mechanisms becoming more important, resulting in a net setup response to roughness. For example, if our experiments were repeated with a

TABLE 3. The instantaneous near-bottom velocity u_b was composed of a near-bottom current U_b and a wave component u_b' that had both asymmetry A_u and skewness S_u (Fig. 7B). The full velocity approximation following Eq. (12) and (13) is presented in row four as well as velocity estimates neglecting 1) u_b' and the contribution of the wave roller mass flux M_r, 2) u_b', and 3) A_u and S_u. These velocity approximations are implemented in various classes of models as indicated in the application column. Large discrepancies in the predicted velocities (Fig. 11) result in variation in the bulk bottom drag coefficients C_d (Fig. 12).

Velocity approximation	Application	C_d
$u_b = U_b$ with $M_r = 0$	Most analytical models	0.23
$u_b = U_b$	Most models including a wave roller	0.067
$u_b = U_b + u_b'$ with $A_u = S_u = 0$	Most phase-averaged models including a wave roller	0.027
$u_b = U_b + u_b'$ with A_u and S_u	Phase-resolving models and some phase-averaged models including a wave roller	0.028

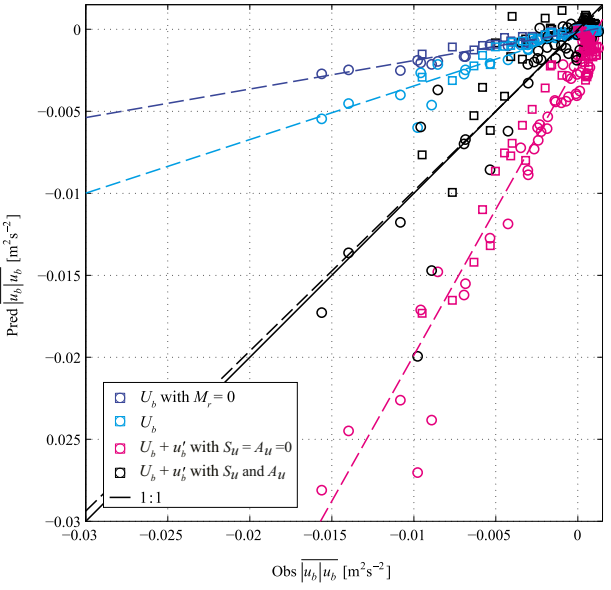

FIG. 12. Comparisons of the observed (obs) and predicted (pred) velocity term $\overline{|u_b|u_b}$ relevant to the calculation of mean bottom stress per Eq. (2) for instrument sites with velocity data on the reef flat. Data are shown for both smooth runs (open circles) and with roughness (open squares). Dashed linear least squares trend lines are shown for each method of predicting velocity (Table 3). The estimated velocity used in this study (shown in black) includes a near-bottom current U_b and a wave component u_b' with velocity asymmetry A_u and skewness S_u.

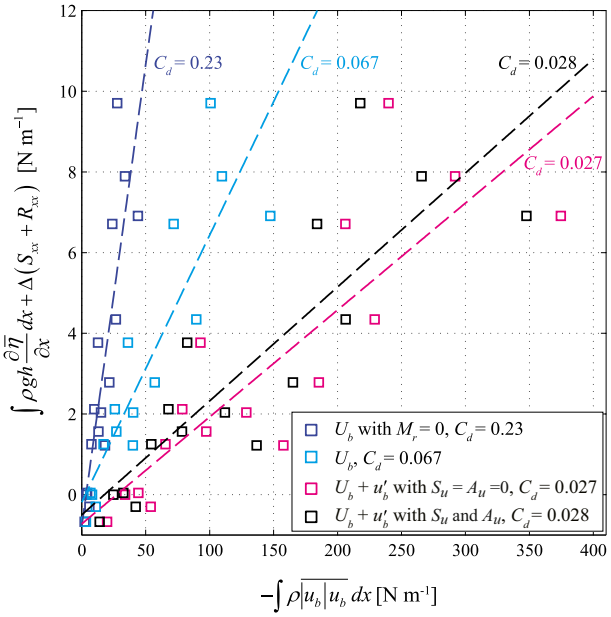

FIG. 13. The velocity approximations given in Table 3 and Fig. 11 were used to compute the cross-shore-integrated time-averaged velocity term in Eq. (16) (x axis) and compared with the sum of the cross-shore-integrated pressure and radiation stress gradients (y axis) for runs with roughness. Per Eq. (16), the linear least squares trend lines (dashed lines) give the estimated bulk bottom drag coefficients C_d for each velocity approximation (values given in legend). The estimated velocity used in this study (shown in black) includes a near-bottom current U_b and a wave component u_b' with velocity asymmetry A_u and skewness S_u.

smooth reef slope and rough reef flat, it is expected that setup would be marginally increased as frictional wave dissipation on the reef slope prior to wave breaking would be reduced (i.e., reducing mechanism 1). Conversely, in the more likely scenario where spatially variable coral die-off on a shallow reef flat results in a smoother reef flat but roughness is maintained on the reef slope (e.g., Quataert et al. 2015), it is expected that setup would decrease. In addition, on slopes steeper than the 1:5 slope used here, the setup response to roughness would be expected to increase, as less frictional wave dissipation would be expected to occur prior to wave breaking. Conversely, on milder reef slopes the opposite could occur. On reefs with open lagoons (i.e., barrier reef systems and atolls) as well as other systems where local continuity does not drive undertows and corresponding offshore-directed mean bottom stresses, it is expected that roughness will reduce setup. As hypothesized by Dean and Bender (2006) in the most extreme example and consistent with the mechanisms we observed, setdown rather than setup would be expected for positively skewed waves interacting with roughness to generate onshore-directed mean bottom stresses in the absence of wave breaking or an undertow.

5. Conclusions

High-resolution laboratory observations were used to investigate the dynamics of wave setup across a fringing reef profile using scaled roughness elements to mimic the large bottom roughness of coral reefs. The 16 offshore wave and still water level conditions were considered, first with a smooth bottom (results detailed in Buckley et al. 2015) and then with a staggered array of cubes mimicking the bulk wave frictional dissipation of reefs. In contrast to previous numerical studies (Apotsos et al. 2007; Franklin et al. 2013), setup on the reef flat for corresponding rough and smooth simulations was found to agree with an average difference of only 7%. The similarity in setup was explained through the detailed assessment of the cross-shore mean momentum balances using the observations, which revealed that roughness both modified radiation stress gradients due to frictional wave dissipation and generated offshore-directed mean bottom stresses. These two mechanisms acted counter to one another, resulting in the observed similarities in setup on the reef flat between rough and smooth runs. When neglecting mean bottom stresses, frictional wave dissipation resulted in radiation stress gradients that were predicted to generate 18% (on average) less setup on the reef flat for rough runs than smooth runs. However, mean bottom stresses for runs with roughness increased the predicted setup by 16% on average compared to neglecting mean bottom stresses. With both frictional wave dissipation and mean bottom stresses accounted for, setup on the reef flat was accurately predicted across all runs with roughness. Comparison of our findings with previous numerical model predictions highlights the need for an improved framework to predict the setup response to both frictional wave dissipation and mean bottom stresses associated with bottom roughness.

Acknowledgments. This project forms part of a Ph.D. study by M. Buckley at The University of Western Australia and is supported by an International Postgraduate Research Scholarship. The experiment was funded by an ARC Future Fellowship Grant (FT110100201) and ARC Discovery Project Grant (DP140102026) to R. J. L. as well as a UWA Research Collaboration Award to R. J. L., M. L. B., and A. V. D. M. L. B. and R. J. L. also acknowledge support through the ARC Centre of Excellence for Coral Reef Studies (CE140100020). Additional funding was provided to A.V.D. by the ''Hydro- and morphodynamics during extreme events'' at Deltares (Project Number 1220002). We also thank Alex Apotsos for helpful discussions. Finally, we thank two anonymous reviewers for their helpful feedback that improved the manuscript.

REFERENCES

Alvarez-Filip, L., N. K. Dulvy, J. A. Gill, I. M. Cote, and A. R. Watkinson, 2009: Flattening of Caribbean coral reefs: Region-wide declines in architectural complexity. *Proc. Roy. Soc. London*, **B276**, 3019–3025, doi:10.1098/rspb.2009.0339.

Apotsos, A., B. Raubenheimer, S. Elgar, R. T. Guza, and J. A. Smith, 2007: Effects of wave rollers and bottom stress on wave setup. *J. Geophys. Res.*, **112**, C02003, doi:10.1029/2006JC003549.

Baldock, T. E., A. Golshani, D. P. Callaghan, M. I. Saunders, and P. J. Mumby, 2014: Impact of sea-level rise and coral mortality on the wave dynamics and wave forces on barrier reefs. *Mar. Pollut. Bull.*, **83**, 155–164, doi:10.1016/j.marpolbul.2014.03.058.

Belcher, S. E., N. Jerram, and J. C. R. Hunt, 2003: Adjustment of a turbulent boundary layer to a canopy of roughness elements. *J. Fluid Mech.*, **488**, 369–398, doi:10.1017/S0022112003005019.

Bouws, E., H. Gunther, W. Rosenthal, and C. L. Vincent, 1985: Similarity of the wind wave spectrum in finite depth water: 1. Spectral form. *J. Geophys. Res.*, **90**, 975–986, doi:10.1029/JC090iC01p00975.

Bowen, A. J., D. L. Inman, and V. P. Simmons, 1968: Wave set-down and set-up. *J. Geophys. Res.*, **73**, 2569–2577, doi:10.1029/JB073i008p02569.

Buckley, M., R. Lowe, J. Hansen, and A. Van Dongeren, 2015: Dynamics of wave setup over a steeply sloping fringing reef. *J. Phys. Oceanogr.*, **45**, 3005–3023, doi:10.1175/JPO-D-15-0067.1.

Chamberlain, J. A., and R. R. Graus, 1975: Water flow and hydromechanical adaptations of branched reef corals. *Bull. Mar. Sci.*, **25**, 112–125.

Dally, W. R., and C. A. Brown, 1995: A modeling investigation of the breaking wave roller with application to cross-shore currents. *J. Geophys. Res.*, **100**, 24 873–24 883, doi:10.1029/95JC02868.

Dean, R. G., and R. A. Dalrymple, 1991: *Water Wave Mechanics for Engineers and Scientists*. Advanced Series on Ocean Engineering, Vol. 2, World Scientific, 368 pp.

——, and C. J. Bender, 2006: Static wave setup with emphasis on damping effects by vegetation and bottom friction. *Coastal Eng.*, **53**, 149–156, doi:10.1016/j.coastaleng.2005.10.005.

Demirbilek, Z., O. G. Nwogu, and D. L. Ward, 2007: Laboratory study of wind effect on runup over fringing reefs. Report 1: Data report. Coastal and Hydraulics Laboratory Rep. ERDC/CHL TR-07-4, 83 pp.

Doering, J. C., and A. J. Bowen, 1995: Parametrization of orbital velocity asymmetries of shoaling and breaking waves using bispectral analysis. *Coastal Eng.*, **26**, 15–33, doi:10.1016/0378-3839(95)00007-X.

Duncan, J. H., 1981: An experimental investigation of breaking waves produced by a towed hydrofoil. *Proc. Roy. Soc. London*, **A377**, 331–348, doi:10.1098/rspa.

Eslami Arab, S., A. van Dongeren, and P. Wellens, 2012: Studying the effect of linear refraction on low-frequency wave propagation (physical and numerical study). *Proc. 33rd Int. Conf. on Coastal Engineering*, Santander, Spain, ASCE, 1–15. [Available online at https://icce-ojs-tamu.tdl.org/icce/index.php/icce/article/view/6710/pdf.]

Falter, J. L., M. J. Atkinson, and M. A. Merrifield, 2004: Mass transfer limitation of nutrient uptake by a wave-dominated reef flat community. *Limnol. Oceanogr.*, **49**, 1820–1831, doi:10.4319/lo.2004.49.5.1820.

Faria, A. F. G., E. B. Thornton, T. P. Stanton, C. V. Soares, and T. C. Lippmann, 1998: Vertical profiles of longshore currents and related bed shear stress and bottom roughness. *J. Geophys. Res.*, **103**, 3217–3232, doi:10.1029/97JC02265.

——, ——, T. C. Lippmann, and T. P. Stanton, 2000: Undertow over a barred beach. *J. Geophys. Res.*, **105**, 16 999–17 010, doi:10.1029/2000JC900084.

Feddersen, F., and R. T. Guza, 2003: Observations of nearshore circulation: Alongshore uniformity. *J. Geophys. Res.*, **108**, 3006, doi:10.1029/2001JC001293.

——, ——, S. Elgar, and T. H. C. Herbers, 2000: Velocity moments in alongshore bottom stress parameterizations. *J. Geophys. Res.*, **105**, 8673–8686, doi:10.1029/2000JC900022.

Franklin, G., I. Marino-Tapia, and A. Torres-Freyermuth, 2013: Effects of reef roughness on wave setup and surf zone currents. *J. Coastal Res.*, **65**, 2005–2010, doi:10.2112/SI65-339.1.

Grant, W. D., and O. S. Madsen, 1979: Combined wave and current interaction with a rough bottom. *J. Geophys. Res.*, **84**, 1797–1808, doi:10.1029/JC084iC04p01797.

Guza, R. T., and E. B. Thornton, 1980: Local and shoaled comparisons of sea surface elevations, pressures, and velocities. *J. Geophys. Res.*, **85**, 1524–1530, doi:10.1029/JC085iC03p01524.

——, and ——, 1981: Wave set-up on a natural beach. *J. Geophys. Res.*, **86**, 4133–4137, doi:10.1029/JC086iC05p04133.

Henderson, S. M., R. T. Guza, S. Elgar, T. H. C. Herbers, and A. J. Bowen, 2006: Nonlinear generation and loss of infragravity wave energy. *J. Geophys. Res.*, **111**, C12007, doi:10.1029/2006JC003539.

Huang, Z. C., L. Lenain, W. K. Melville, J. H. Middleton, B. Reineman, N. Statom, and R. M. McCabe, 2012: Dissipation of wave energy and turbulence in a shallow coral reef lagoon. *J. Geophys. Res.*, **117**, C03015, doi:10.1029/2011JC007202.

Jadhav, R. S., Q. Chen, and J. M. Smith, 2013: Spectral distribution of wave energy dissipation by salt marsh vegetation. *Coastal Eng.*, **77**, 99–107, doi:10.1016/j.coastaleng.2013.02.013.

Jonsson, I. G., 1966: Wave boundary layers and friction factors. *Proc. 10th Conf. on Coastal Engineering*, Tokyo, Japan, ASCE, 127–148. [Available online at https://icce-ojs-tamu.tdl.org/icce/index.php/icce/article/view/2423/2090.]

Lentz, S. J., M. Fewings, P. Howd, J. Fredericks, and K. Hathaway, 2008: Observations and a model of undertow over the inner continental shelf. *J. Phys. Oceanogr.*, **38**, 2341–2357, doi:10.1175/2008JPO3986.1.

Longuet-Higgins, M. S., 1970: Longshore currents generated by obliquely incident sea waves: 1. *J. Geophys. Res.*, **75**, 6778–6789, doi:10.1029/JC075i033p06778.

——, 2005: On wave set-up in shoaling water with a rough sea bed. *J. Fluid Mech.*, **527**, 217–234, doi:10.1017/S0022112004003222.

——, and R. W. Stewart, 1962: Radiation stress and mass transport in gravity waves, with application to 'surf beats.' *J. Fluid Mech.*, **13**, 481–504, doi:10.1017/S0022112062000877.

——, and ——, 1964: Radiation stresses in water waves; a physical discussion, with applications. *Deep-Sea Res. Oceanogr. Abstr.*, **11**, 529–562, doi:10.1016/0011-7471(64)90001-4.

Lowe, R. J., and J. L. Falter, 2015: Oceanic forcing of coral reefs. *Annu. Rev. Mar. Sci.*, **7**, 43–66, doi:10.1146/annurev-marine-010814-015834.

——, ——, M. D. Bandet, G. Pawlak, M. J. Atkinson, S. G. Monismith, and J. R. Koseff, 2005a: Spectral wave dissipation over a barrier reef. *J. Geophys. Res.*, **110**, C04001, doi:10.1029/2004JC002711.

——, J. R. Koseff, and S. G. Monismith, 2005b: Oscillatory flow through submerged canopies: 1. Velocity structure. *J. Geophys. Res.*, **110**, C10016, doi:10.1029/2004JC002788.

——, J. L. Falter, J. R. Koseff, S. G. Monismith, and M. J. Atkinson, 2007: Spectral wave flow attenuation within submerged canopies:

Implications for wave energy dissipation. *J. Geophys. Res.*, **112**, C05018, doi:10.1029/2006JC003605.

——, U. Shavit, J. L. Falter, J. R. Koseff, and S. G. Monismith, 2008: Modeling flow in coral communities with and without waves: A synthesis of porous media and canopy flow approaches. *Limnol. Oceanogr.*, **53**, 2668–2680, doi:10.4319/lo.2008.53.6.2668.

——, J. L. Falter, S. G. Monismith, and M. J. Atkinson, 2009a: Wave-driven circulation of a coastal reef–lagoon system. *J. Phys. Oceanogr.*, **39**, 873–893, doi:10.1175/2008JPO3958.1.

——, ——, ——, and ——, 2009b: A numerical study of circulation in a coastal reef-lagoon system. *J. Geophys. Res.*, **114**, C06022, doi:10.1029/2008JC005081.

——, C. Hart, and C. B. Pattiaratchi, 2010: Morphological constraints to wave-driven circulation in coastal reef-lagoon systems: A numerical study. *J. Geophys. Res.*, **115**, C09021, doi:10.1029/2009JC005753.

Luhar, M., S. Coutu, E. Infantes, S. Fox, and H. Nepf, 2010: Wave-induced velocities inside a model seagrass bed. *J. Geophys. Res.*, **115**, C12005, doi:10.1029/2010JC006345.

Macdonald, R. W., 2000: Modelling the mean velocity profile in the urban canopy layer. *Bound.-Layer Meteor.*, **97**, 25–45, doi:10.1023/A:1002785830512.

Mei, C. C., M. Stiassnie, and D. K.-P. Yue, 2005: *Theory and Applications of Ocean Surface Waves. Part 2: Nonlinear Aspects*. World Scientific, 1071 pp.

Monismith, S. G., 2007: Hydrodynamics of coral reefs. *Annu. Rev. Fluid Mech.*, **39**, 37–55, doi:10.1146/annurev.fluid.38.050304.092125.

——, L. M. M. Herdman, S. Ahmerkamp, and J. L. Hench, 2013: Wave transformation and wave-driven flow across a steep coral reef. *J. Phys. Oceanogr.*, **43**, 1356–1379, doi:10.1175/JPO-D-12-0164.1.

——, J. S. Rogers, D. Koweek, and R. B. Dunbar, 2015: Frictional wave dissipation on a remarkably rough reef. *Geophys. Res. Lett.*, **42**, 4063–4071, doi:10.1002/2015GL063804.

Nelson, R. C., 1996: Hydraulic roughness of coral reef platforms. *Appl. Ocean Res.*, **18**, 265–274, doi:10.1016/S0141-1187(97)00006-0.

Nepf, H. M., and E. R. Vivoni, 2000: Flow structure in depth-limited, vegetated flow. *J. Geophys. Res.*, **105**, 28 547–28 557, doi:10.1029/2000JC900145.

Nielsen, P., 1992: *Coastal Bottom Boundary Layers and Sediment Transport*. Advanced Series on Ocean Engineering, Vol. 4, World Scientific, 340 pp.

Pequignet, A. C. N., J. M. Becker, and M. A. Merrifield, 2014: Energy transfer between wind waves and low-frequency oscillations on a fringing reef, Ipan, Guam. *J. Geophys. Res. Oceans*, **119**, 6709–6724, doi:10.1002/2014JC010179.

Quataert, E., C. Storlazzi, A. van Rooijen, O. Cheriton, and A. van Dongeren, 2015: The influence of coral reefs and climate change on wave-driven flooding of tropical coastlines. *Geophys. Res. Lett.*, **42**, 6407–6415, doi:10.1002/2015GL064861.

Raubenheimer, B., R. T. Guza, and S. Elgar, 2001: Field observations of wave-driven setdown and setup. *J. Geophys. Res.*, **106**, 4629–4638, doi:10.1029/2000JC000572.

Roberts, H. H., S. P. Murray, and J. N. Suhayda, 1975: Physical processes in a fringing reef system. *J. Mar. Res.*, **33**, 233–260.

Rosman, J. H., and J. L. Hench, 2011: A framework for understanding drag parameterizations for coral reefs. *J. Geophys. Res.*, **116**, C08025, doi:10.1029/2010JC006892.

Ruessink, B. G., G. Rarnaekers, and L. C. van Rijn, 2012: On the parameterization of the free-stream non-linear wave orbital motion in nearshore morphodynamic models. *Coastal Eng.*, **65**, 56–63, doi:10.1016/j.coastaleng.2012.03.006.

Sheppard, C., D. J. Dixon, M. Gourlay, A. Sheppard, and R. Payet, 2005: Coral mortality increases wave energy reaching shores protected by reef flats: Examples from the Seychelles. *Estuarine Coastal Shelf Sci.*, **64**, 223–234, doi:10.1016/j.ecss.2005.02.016.

Stive, M. J. F., and H. G. Wind, 1982: A study of radiation stress and set-up in the nearshore region. *Coastal Eng.*, **6**, 1–25, doi:10.1016/0378-3839(82)90012-6.

——, and H. J. De Vriend, 1994: Shear stresses and mean flow in shoaling and breaking waves. *Proc. 24th Int. Conf. on Coastal Engineering*, Kobe, Japan, ASCE, 594–608, doi:10.1061/9780784400890.045.

Svendsen, I. A., 1984: Wave heights and set-up in a surf zone. *Coastal Eng.*, **8**, 303–329, doi:10.1016/0378-3839(84)90028-0.

——, 2006: *Introduction to Nearshore Hydrodynamics*. Advanced Series on Ocean Engineering, Vol. 24, World Scientific, 744 pp.

van Dongeren, A., G. Klopman, A. Reniers, and H. Petit, 2002: High-quality laboratory wave generation for flumes and basins. *Ocean Wave Measurement and Analysis* (2001), B. L. Edge and J. M. Hemsley, Eds., American Society of Civil Engineers, 1190–1199, doi:10.1061/40604(273)120.

——, R. Lowe, A. Pomeroy, D. M. Trang, D. Roelvink, G. Symonds, and R. Ranasinghe, 2013: Numerical modeling of low-frequency wave dynamics over a fringing coral reef. *Coastal Eng.*, **73**, 178–190, doi:10.1016/j.coastaleng.2012.11.004.

Zeller, R. B., F. J. Zarama, J. S. Weitzman, and J. R. Koseff, 2015: A simple and practical model for combined wave–current canopy flows. *J. Fluid Mech.*, **767**, 842–880, doi:10.1017/jfm.2015.59.